

VoroLight: Learning Quality Volumetric Voronoi Meshes from General Inputs

Jiayin Lu^{1*} Ying Jiang^{1*} Yin Yang² Chenfanfu Jiang¹



Figure 1: VoroLight generates high-quality volumetric Voronoi meshes for artistic 3D printed lamps. Our method produces watertight, topologically consistent Voronoi meshes from general inputs, enabling applications such as artistic lamp design. Shown here: (a) sphere lamp, (b) cow lamp, (c) bunny lamp, and (d) heart lamp.

Abstract

We present VoroLight, a differentiable framework for 3D shape reconstruction based on Voronoi meshing. Our approach generates smooth, watertight surfaces and topologically consistent volumetric meshes directly from diverse inputs, including images, implicit shape level-set fields, point clouds and meshes. VoroLight operates in three stages: it first initializes a surface using a differentiable Voronoi formulation, then refines surface quality through a polygon-face sphere training stage, and finally reuses the differentiable Voronoi formulation for volumetric optimization with additional interior generator points. Project page: <https://jiayinlu19960224.github.io/>

* equal contribution. ¹ UCLA, ² University of Utah. jiayin_lu@ucla.edu, yingjiang@cffjiang@ucla.edu, yin.yang@utah.edu

[vorolight/](https://github.com/vorolight/)

1. Introduction

Reconstructing 3D shapes from diverse data sources, such as images, point clouds, implicit shape level-set fields (e.g. signed distance fields), or surface meshes, remains an important research problem in computer graphics, geometry processing, and computational design. A high-quality reconstruction should faithfully capture shape geometry. To support applications in simulation, analysis, and fabrication, a topologically consistent volumetric structure is further required.

Recent advances in generative models have enabled methods that produce impressive surface meshes from various inputs, including multi-view images, point clouds, and even text prompts [9, 13, 15]. However, these meshes typically lack internal volumetric structure and are often non-

watertight or self-intersecting, which limits their utility in physically grounded applications [18]. Broadly, existing 3D reconstruction techniques fall into two categories: *surface reconstruction* [13, 15, 28], which focuses on recovering shape boundaries but usually omits volumetric connectivity, and *volumetric meshing* [1], which constructs interior structure but commonly relies on clean surface inputs or fixed discretizations (e.g., grid-, voxel-, or tetrahedral-template-based representations) that restrict geometric flexibility.

Voronoi diagrams naturally produce convex, watertight, and topologically consistent cells [1, 18], making them well-suited for downstream physical applications. Our goal is to develop a learnable, general-purpose Voronoi meshing framework that can generate simulation-ready Voronoi diagrams directly from multimodal inputs. We introduce *VoroLight*, a differentiable pipeline that optimizes Voronoi structures directly from general shape inputs through gradient-based learning, and produces high-quality, watertight volumetric meshes with well-regularized, smooth surfaces. It operates through three sequential stages: (1) differentiable Voronoi surface initialization from the input modality, (2) polygon-face sphere training for surface refinement that enforces local geometric constraints, and (3) volumetric optimization that introduces internal generator points to obtain a volumetric mesh with globally consistent topology.

Our main contributions are as follows:

- We present *VoroLight*, a differentiable three-stage Voronoi reconstruction framework that generates watertight volumetric meshes with smooth surface and consistent topology from diverse inputs, including implicit shape level-set fields, point clouds, meshes, and images.
- We introduce a polygon-face sphere training formulation that extends sphere-based Voronoi surface construction to a differentiable setting, enabling self-regularized and high-quality surface refinement.
- We demonstrate the versatility of our framework through applications in artistic Voronoi lamp design and single-image 3D shape generation tasks.

2. Related Work

2.1. 3D Shape Reconstruction

3D shape reconstruction has been extensively studied across different input modalities, including meshes [18], SDFs [29], point clouds [7, 10], and images [9, 14, 15, 32]. Existing methods can be broadly categorized by their output representation, either triangle-based surface meshes [10, 14, 15] or volumetric tetrahedral meshes [9].

Surface reconstruction methods [14, 15] typically learn to generate triangle meshes directly from geometric or image inputs. However, such models often produce non-watertight or self-intersecting surfaces, which hinder downstream physical simulation and volumetric meshing [18].

In volumetric reconstruction, classical algorithms such as *TetGen* [26] construct high-quality tetrahedral meshes from Piecewise Linear Complexes (PLCs) using Delaunay refinement with provable geometric guarantees. While robust for clean surface inputs, these methods lack differentiability and adaptability to noisy or implicit data. *TetSphere* [9] represents shapes as unions of deformable tetrahedral “TetSpheres” to produce high-quality volumetric reconstructions, but the method yields only piecewise patches rather than a globally consistent mesh, resulting in overlaps and inconsistent internal topology.

2.2. Neural Implicit Representations and Hybrid Methods

Learning-based approaches increasingly represent 3D shapes as neural implicit functions [8, 19, 22] or hybrid representations combining implicit fields with explicit mesh extraction [3, 25]. *DeepSDF* [22] and *Occupancy Networks* [19] learn continuous shape representations but require post-processing (e.g., Marching Cubes) to extract surfaces, often producing irregular triangle meshes without volumetric structure. *DMTet* [25] addresses this by combining neural SDFs with differentiable marching tetrahedra, enabling end-to-end learning with tetrahedral topology. However, it extracts surface meshes from a background tetrahedral grid structure, where the volumetric tessellation does not conform to the shape’s geometry. *FlexiCubes* [3] extends this with dual marching cubes for improved isosurface quality but similarly outputs triangle meshes without shape-conforming volumetric cells.

2.3. Voronoi-Based Meshing

Voronoi-based meshing provides convex, non-overlapping polyhedral cells ideal for finite-volume and physics-based simulation, with orthogonal face–edge structure that improves numerical stability [1, 18, 31]. Voronoi faces defined between oppositely labeled generators enable watertight, non-self-intersecting surface reconstruction from unstructured inputs [18]. However, standard Voronoi diagrams are unbounded and do not naturally conform to geometric boundaries, often requiring ad-hoc clipping or trimming that compromises convexity.

VoroCrust [1] addresses this with a provably correct sphere-based construction of boundary-conforming volumetric Voronoi meshes without cell clipping. It wraps the input triangle surface mesh in a union of spheres centered at mesh vertices. These spheres approximate the surface and encodes sharp features. For each face, Voronoi generators are placed in pairs at triple-sphere intersections so that their bisectors reproduce the input facets, yielding cells with strong feature preservation. However, *VoroCrust* is a deterministic, non-learning method limited to fixed triangular mesh surface inputs and does not support adaptive or

differentiable refinement.

Variational optimization of Voronoi structures has been explored through restricted Voronoi energy minimization [20] and anisotropic Optimal Power Diagrams [31], but these methods do not support differentiable, boundary-aware volumetric reconstruction.

2.4. Differentiable Voronoi Learning

Recent work has explored differentiable formulations of Voronoi structures, enabling gradient optimization and data-driven reconstruction.

VoroMesh [18] optimizes generator positions to construct a Voronoi surface mesh conforming to an input point cloud. Watertight surfaces are defined as Voronoi faces between oppositely labeled generators. These in-between faces correspond exactly to bisector planes between generator points. *VoroMesh* introduces a *VoroLoss* that approximates point-to-bisector distances, allowing gradient-based training without explicitly constructing the full Voronoi diagram. As the first learning-based Voronoi meshing framework, *VoroMesh* successfully bridges geometric Voronoi theory and data-driven surface reconstruction. However, the framework is limited to surface reconstruction, point cloud inputs, and lacks explicit surface smoothness regularization.

Differentiable Voronoi Diagrams [21] introduce a closed-form, differentiable formulation of Voronoi vertices with respect to generator positions, allowing Newton-type optimization to simulate cellular and foam-like materials. This implicit formulation allows continuous topology changes, including cell division and merging, without explicit re-meshing or contact handling. Although designed for physical simulation, it provides a strong differentiable geometric foundation for Voronoi-based optimization.

3. Method

We generate high-quality, watertight volumetric Voronoi meshes from general inputs by optimizing differentiable Voronoi formulations.

Our framework consists of three sequential stages (Fig. 2). In stage I, we use the *differentiable Voronoi diagram* to learn an initial Voronoi surface – characterized by uniformly sized, rounded faces – that approximates the target shape. In stage II, to refine the initial surface to a smooth, shape-conforming Voronoi geometry, we extend *VoroCrust*’s sphere-based Voronoi reconstruction into a differentiable, learnable formulation. The vertices of each surface face are associated with a trainable sphere, parameterized by its center and radius, while each face also has a trainable offset that determines the locations of two intersection points. By forcing spheres incident to the same face to pass through the two intersection points of the face, these parameters allow the surface to self-regularize into a smooth and uniform Voronoi surface through learning

Stage	\mathcal{L}_{reg}	$\mathcal{L}_{\text{shape}}$	$\mathcal{L}_{\text{sphere}}$	\mathcal{L}_{CVT}
Stage I	✓	✓	–	–
Stage II	✓	✓	✓	–
Stage III	–	–	–	✓

Table 1. Loss terms used in each training stage.

rather than rule-based refinement. Stage III keeps the refined surface generators fixed and introduces interior generators, optimized under a centroidal Voronoi tessellation (CVT) [6] loss for uniform and topologically consistent volumetric meshing.

In Stage II, we consider two variants: (i) subdividing the resultant Voronoi polygon faces from Stage I into triangles (by connecting face vertices to face centroids) and applying sphere constraints on these triangular faces; and (ii) applying sphere constraints directly on the general polygon faces. Empirically, triangle-face sphere training yields higher-quality surfaces, and is therefore used as default in the pipeline. The polygon-face variant is used for artistic Voronoi lamp designs in Sec. 5.2.

Each stage uses a specific combination of task-dependent losses (Table 1); detailed formulations are given in Sec. 3.4 and the supplementary material.

3.1. Stage I: Initial Polygon Surface

Initialization. We initialize generators via boundary-reflection. We first generate a uniform cubic voxel grid, where each voxel is categorized to be interior or exterior of the shape. The grid resolution is controlled by parameter n_{init} , which specifies the number of grid cells along the longest side of the shape. The length of voxel edge gives the characteristic lengthscale h_0 . We dilate three layers outwards of the interior mask to obtain an exterior boundary band. Exterior boundary generators are placed at band voxel centers. For each, we compute a Gaussian-smoothed normal from the interior mask and reflect inward to generate a corresponding interior generator near the surface. We build an initial Voronoi diagram and discard inner generators whose cells do not intersect the boundary. See supplementary material for complete details.

Differentiable Voronoi Surface. Following [21], a Voronoi vertex v_c induced by four generators x_i , $i \in \{0, 1, 2, 3\}$, is

$$v_c = \frac{1}{2} A^{-1} \mathbf{b}, \quad A = \begin{bmatrix} (\mathbf{x}_1 - \mathbf{x}_0)^\top \\ (\mathbf{x}_2 - \mathbf{x}_0)^\top \\ (\mathbf{x}_3 - \mathbf{x}_0)^\top \end{bmatrix}, \quad \mathbf{b} = \begin{bmatrix} \|\mathbf{x}_1\|^2 - \|\mathbf{x}_0\|^2 \\ \|\mathbf{x}_2\|^2 - \|\mathbf{x}_0\|^2 \\ \|\mathbf{x}_3\|^2 - \|\mathbf{x}_0\|^2 \end{bmatrix}. \quad (1)$$

This closed form enables back-propagation from vertex-based losses to generator positions. We extract the surface

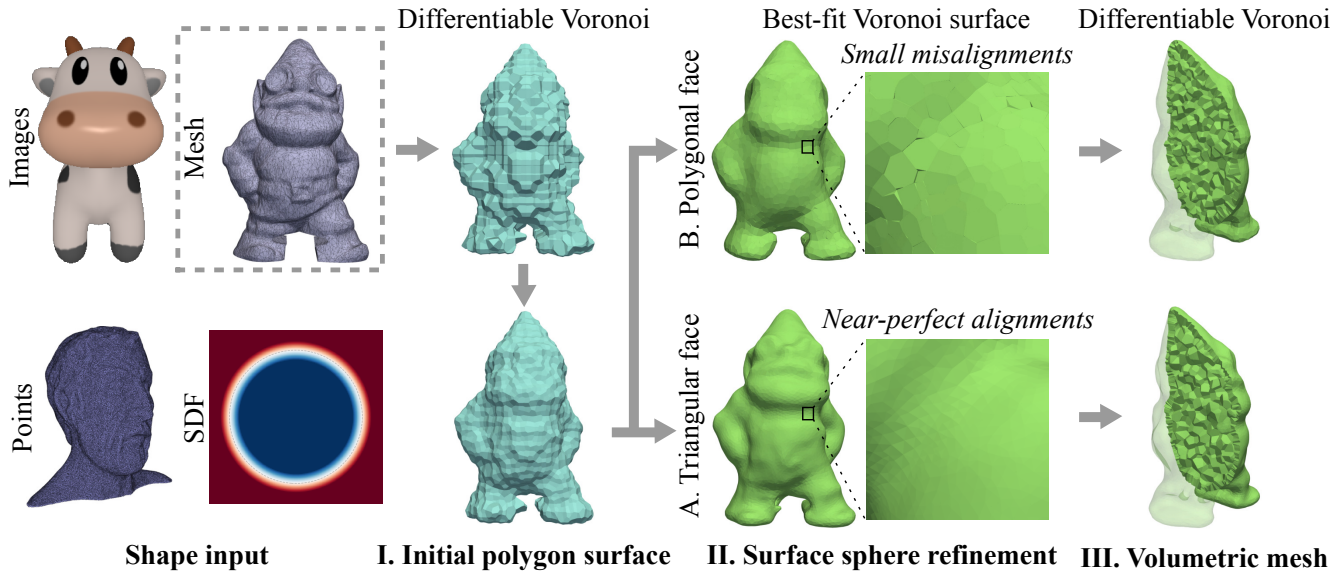


Figure 2. **VoroLight pipeline.** *VoroLight* generates smooth, watertight volumetric Voronoi meshes from general inputs via a three-stage pipeline. Stage I learns a differentiable Voronoi surface from the target shape. Stage II refines this surface using trainable sphere centers, radii, and per-face offsets: polygon-face constraints form a globally over-constrained system with small residuals, while triangle-face constraints are locally consistent and yield near-perfect alignments between surface faces. Stage III fixes the refined surface and optimizes additional interior generators under a CVT loss to obtain a quality volumetric tessellation. The example shown here uses $n_{\text{init}} = 25$, $N_{\text{inner}} = 800$.

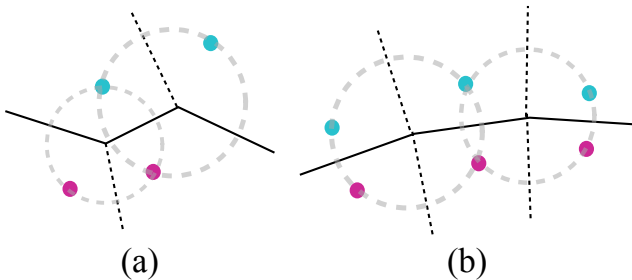


Figure 3. Schematic plot in 2D of (a) a stable Voronoi configuration and (b) a degenerate Voronoi diagram.

as Voronoi faces separating inner and outer generators. During optimization, we adaptively remesh when generators have large movements. Additional details are given in the supplementary material.

Stage I optimizes a combination of shape and regularization losses, promoting smoothness and uniformity while fitting the target geometry. The resulting surface faces are uniformly sized and rounded.

However, the resulting surface exhibits noticeable bumpiness rather than smoothness. This effect arises from the intrinsic stability configuration of a standard Voronoi diagram. As illustrated in a 2D example in Fig. 3, a stable Voronoi vertex is defined by the intersection of three

generator bisectors. When four or more generators meet at a single vertex, the configuration becomes degenerate and unstable; yet such degenerate configurations are precisely what enable the formation of a smooth, continuously curved surface.

In three dimensions, a stable Voronoi vertex arises from the intersection of four cells, while intersections involving five or more cells are degenerate. The absence of these higher-order intersections causes the reconstructed 3D surface to appear locally uneven rather than smooth and continuous.

3.2. Stage II: Surface Sphere Refinement

To obtain smooth Voronoi surfaces, we introduce a differentiable face-sphere formulation extending *VoroCrust* [1]. For each surface Voronoi vertex v we define a trainable sphere $S_v = (\mathbf{c}_v, r_v)$, with center \mathbf{c}_v initialized at the Stage I surface vertex and radius r_v from local geometry (average distance to incident face centroids). For each face f we introduce a learnable offset δ_f (initialized as $\sqrt{A_f}$, where A_f is the face area) that defines two intersection points

$$\mathbf{p}_f^{(1)} = \mathbf{c}_f + \delta_f \mathbf{n}_f, \quad \mathbf{p}_f^{(2)} = \mathbf{c}_f - \delta_f \mathbf{n}_f, \quad (2)$$

where \mathbf{c}_f and \mathbf{n}_f are the face centroid and face unit normal. The uniformly sized and rounded faces produced by Stage I provide an ideal initialization for this sphere-based

refinement.

Constraining the intersection points to $\mathbf{c}_f \pm \delta_f \mathbf{n}_f$ reduces the configuration to one scalar per face, improving regularity and numerical stability. This centroid-based formulation keeps intersections symmetric, avoiding skewed configurations and promoting smoothly varying sphere arrangements. Our formulation biases the solution toward rounded, convex faces while discouraging elongated, thin, or concave ones.

The final Voronoi surface is reconstructed from the optimized intersection points by computing the Voronoi diagram and extracting the boundary surface.

We optimize $\{\mathbf{c}_v, r_v, \delta_f\}$ under two geometric constraints using power distance $g(\mathbf{p}, \mathbf{c}, r) = \|\mathbf{p} - \mathbf{c}\|^2 - r^2$:

Intersection loss. Spheres incident to face f must pass through $\mathbf{p}_f^{(1)}$ and $\mathbf{p}_f^{(2)}$:

$$\mathcal{L}_{\text{int}} = \frac{1}{2N_{\text{pairs}}} \sum_f \sum_{v \in V(f)} \sum_{k=1,2} [g(\mathbf{p}_f^{(k)}, \mathbf{c}_v, r_v)]^2, \quad (3)$$

where $V(f)$ is the set of vertices incident to f and $N_{\text{pairs}} = \sum_f |V(f)|$.

Exclusion loss. Non-incident spheres must not enclose the intersection points:

$$\mathcal{L}_{\text{excl}} = \frac{1}{N_{\text{viol}}} \sum_f \sum_{v \notin V(f)} \sum_{k=1,2} [\max(0, m - g(\mathbf{p}_f^{(k)}, \mathbf{c}_v, r_v))]^2, \quad (4)$$

where $m = 10^{-13}$ and N_{viol} counts actual violations. A KD-tree accelerates non-incident sphere queries.

The total loss is $\mathcal{L}_{\text{sphere}} = \mathcal{L}_{\text{int}} + \mathcal{L}_{\text{excl}}$, combined with shape and regularization losses.

Polygon vs. triangle faces. For general polygon faces, each sphere participates in multiple neighboring faces, and in many faces $n > 3$ spheres are required to intersect at exactly two shared intersection points, which is locally over-constrained. Furthermore, enforcing $n > 3$ vertices of an n -gon to share a common bisector plane biases the solution toward locally planar configurations, smoothing curvature and weakening sharp features. As a result, polygon-face sphere training produces a globally over-constrained system where shape and sphere constraints compete, and the best-fit Voronoi surface tends to smooth out features and has slight misalignments between adjacent faces.

In contrast, when faces are restricted to triangles, each local system involves exactly three spheres and two intersection points. Three intersecting spheres in general position naturally intersect along a curve passing through two consistent points, making the constraints locally realizable.

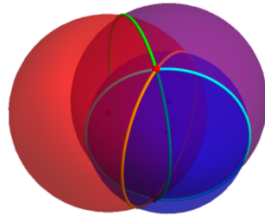


Figure 4. Intersection of three spheres in general position. Visualization generated using Mathematica code by Erik Mahieu [17].

As shown in Fig. 4, each pair of the three spheres

(i, j) defines a *radical plane*

$\{\mathbf{x} : \|\mathbf{x} - \mathbf{c}_i\|^2 - \|\mathbf{x} - \mathbf{c}_j\|^2 = r_i^2 - r_j^2\}$, and the intersection of any two radical planes forms the *radical line*. This line intersects the third sphere at two points, which simultaneously satisfy $\|\mathbf{x} - \mathbf{c}_i\|^2 = r_i^2$ for $i = 1, 2, 3$. These two intersection points (one highlighted in red) represent the locally consistent geometric solutions underlying the triangle-face sphere formulation.

Moreover, the three vertices of a triangle are inherently coplanar, so the corresponding sphere constraints are compatible without over-constraining the system. This yields significantly smaller residuals in optimization, near-perfect boundary face alignments, and smoother, more feature-preserving surfaces.

Consequently, we adopt triangle-face sphere training as the default refinement strategy, and use polygon-face sphere training primarily for artistic Voronoi lamp designs.

3.3. Stage III: Volumetric Mesh

Given the refined surface from Stage II, we fix surface generators (inner and outer) and introduce N_{inner} deep interior generators to fill the volume. Deep interior generators are obtained through an iterative Voronoi-verified sampling procedure that ensures added points do not alter the optimized Voronoi surface from Stage II (details in supplementary material). Candidate points are randomly sampled within the mesh bounding box and iteratively filtered by computing Voronoi diagrams with the surface generators, removing any candidates whose Voronoi cells would intersect the surface. The deep interior generators are then optimized under a CVT loss \mathcal{L}_{CVT} (see the supplementary material) that encourages each generator to coincide with its cell centroid, promoting uniform volumetric partitioning [6]. This produces a watertight volumetric Voronoi mesh with consistent surface-interior connectivity.

3.4. Loss Functions

Shape losses align the Voronoi surface with the target geometry. For implicit inputs (e.g., signed distance fields), we minimize the squared implicit level-set error. For point cloud inputs, we use a fast bidirectional Chamfer distance between points sampled on the *VoroLight* mesh surface and the target point cloud. For mesh inputs, we densely sample surface points for a target point cloud and apply the same Chamfer distance loss. For image inputs, we minimize rasterized silhouette, normal, and shading differences.

Regularization losses promote smooth, well-shaped surfaces. They include normal consistency (penalizes angular deviation between neighboring faces), area uniformity (reduces face area variance), cell circularity (encourages round faces), centroid alignment (penalizes the distance be-

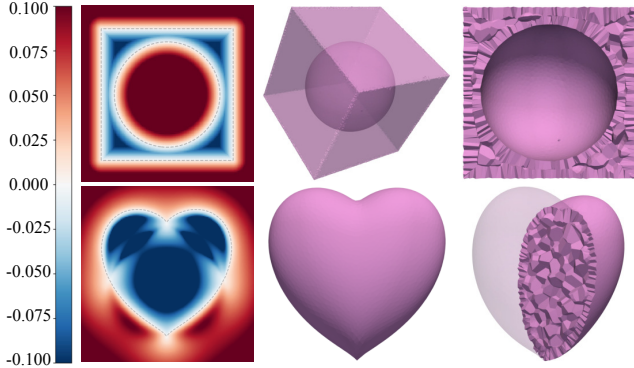


Figure 5. Cube with spherical cavity SDF, Taubin heart implicit field, and their Voronoi reconstruction. The example shown here uses $n_{\text{init}} = 15$ and $N_{\text{inner}} = 800$.

tween each face centroid and the average centroid of its neighboring faces), and Laplacian smoothness (local vertex averaging).

All regularization terms are normalized using the mean face area \bar{A} . Complete mathematical definitions of all loss terms are given in the supplementary.

4. Experiments

We demonstrate the versatility of *VoroLight* across four input modalities: implicit shape level-set fields, surface meshes, point clouds, and multi-view images. All experiments use the same three-stage pipeline described in Sec. 3 and employ the triangle-face sphere refinement in Stage II. We construct a testing dataset comprising 22 object meshes: 10 meshes without texture information randomly selected from Thing10K [33], and 12 meshes with texture information, including 11 randomly selected from Objaverse [5] and the Spot model [4]. We use PyTorch3D [23] and neural deferred shader (NDS) [30] to extract dense surface target point clouds and multi-view RGB and normal field image inputs under consistent camera poses. We further develop a Python binding for the multi-threaded *Voro++* library [16, 24] to efficiently compute Voronoi diagrams within our pipeline.

4.1. Implicit Shape Level-Set Field

We validate *VoroLight* on analytic implicit fields, whose zero level set defines continuous surfaces.

We test two implicit shapes: the Taubin heart [27], and a cube with a spherical cavity constructed via signed distance field (SDF) composition.

The Taubin heart is defined as

$$F(x, y, z) = (x^2 + \frac{9}{4}y^2 + z^2 - 1)^3 - x^2z^3 - \frac{9}{80}y^2z^3 = 0.$$

The cube-sphere shape is formed using

$$F(x, y, z) = \max(F_{\text{cube}}, -F_{\text{sphere}}),$$

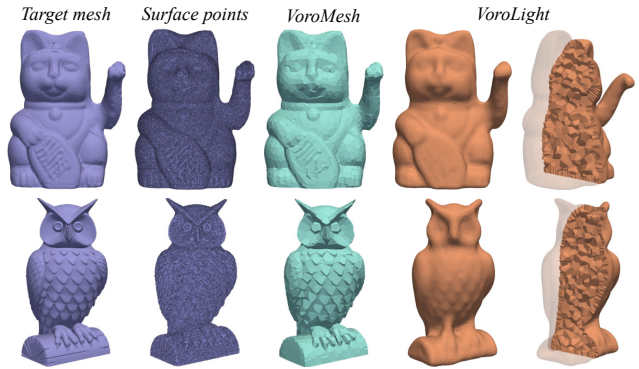


Figure 6. **Comparison with *Voromesh*** on shape reconstruction from surface point clouds with 153,600 points each. The example shown here uses $n_{\text{init}} = 25$ and $N_{\text{inner}} = 800$.

where $F_{\text{cube}}(x, y, z) = \frac{1}{2}(\max(|x|, |y|, |z|) - a)$ and $F_{\text{sphere}}(x, y, z) = \sqrt{x^2 + y^2 + z^2} - r$.

Figure 5 shows, from left to right: 2D slices of the input implicit shape fields (blue: interior, red: exterior), the Voronoi surfaces reconstructed through sphere-based optimization (Stage II), and the final volumetric Voronoi tessellations (Stage III), forming watertight and convex-cell meshes. Along sharp edges, the Voronoi faces exhibit misalignments because the face spheres must simultaneously satisfy constraints from incident adjacent faces that are non-smooth with discontinuous normals. With uniform generator density and shape smoothness regularization, the optimization converges to a compromised configuration rather than an exact fit at the crease. As future work, a feature-aware, adaptively refined generator distribution along sharp edges or high-curvature regions could provide additional degrees of freedom to better resolve these challenging features.

4.2. Surface Mesh and Point Cloud

For input surface meshes, we reformulate the task as reconstructing the shape from a point cloud. We test on the 10 Thing10K objects from our dataset, uniformly sampling a dense set of points on the ground-truth mesh surface to use as the target point cloud. We supervise reconstruction using a fast bidirectional Chamfer distance between points sampled on the *VoroLight* surface and points sampled on the target mesh surface, with nearest neighbors efficiently computed via KNN search. This point-based formulation is more efficient than repeatedly querying distances from points on the Voronoi surface to faces of the target mesh, while still accurately capturing underlying shape geometry.

We compare the reconstructed meshes against *VoroMesh* [18]. As shown in Fig. 6, both *VoroLight* and *VoroMesh* generate watertight surfaces. While *VoroMesh* preserves finer geometric details of the original shape, it exhibits slight misalignments between adjacent

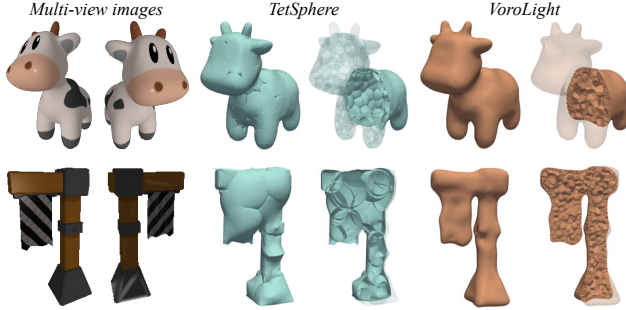


Figure 7. **Comparison with *TetSphere Splatting*** on multi-view image reconstruction. Each model is reconstructed from 300 input views. The example shown here uses $n_{\text{init}} = 40$ and $N_{\text{inner}} = 100$.

faces. In contrast, *VoroLight* produces smoother surface meshes with near-perfect Voronoi face alignments, and its triangle elements are well-shaped, close to equilateral triangles. The triangle-face sphere refinement procedure, combined with the imposed surface regularization losses, enhances the regularity and normal consistency of the resulting mesh, albeit at a slight cost of smoothing out fine geometric details. Table 2 presents quantitative results over the 10 Thingi10K shapes. *VoroMesh* achieves lower mean squared Chamfer distance and a higher F1 score, indicating superior geometric accuracy. Nevertheless, in comparison, *VoroLight* offers smoother and more regular surfaces and further extends naturally to full volumetric tessellation.

Method	Mean CD ² ($\times 10^{-3}$)	Mean F1
<i>VoroLight</i>	0.0422 \pm 0.0329	0.9664 \pm 0.0427
<i>VoroMesh</i>	0.0101 \pm 0.0035	0.9997 \pm 0.0008

Table 2. Mean squared Chamfer distance and F1 score on the 10 Thingi10K samples comparing *VoroMesh* and *VoroLight*.

4.3. Multi-view Images

Finally, we compare *VoroLight* with *TetSphere Splatting* [9] on multi-view image reconstruction (Fig. 7). We use the 12 textured meshes from our dataset, and render 300 views for each, including corresponding depth and normal maps. *TetSphere* is trained with silhouette and depth supervision, and subsequently optimized with shading to recover texture. In contrast, *VoroLight* first obtains geometry with silhouette and normal-map supervision rendered using the differentiable rasterizer *nvdiffrast* [12]. The geometry is then kept fixed, and a *neural deferred shader (NDS)* [30] is trained with a shading loss to obtain the target appearance.

TetSphere represents shapes using locally volumetric tetrahedral meshes organized as disconnected tetrahedral clusters, without enforcing a global volumetric structure, which can leave holes between clusters. In contrast, *Voro-*

Light reconstructs watertight volumetric meshes with globally consistent topology. Quantitatively, as shown in Table 3, *VoroLight* achieves substantially lower mean squared Chamfer distance and a higher F1 score than *TetSphere*, indicating improved geometric accuracy and better surface consistency across the reconstructed shapes.

Method	Mean CD ² ($\times 10^{-3}$)	Mean F1
<i>VoroLight</i>	1.3149 \pm 1.2697	0.5150 \pm 0.1929
<i>TetSphere</i>	3.6539 \pm 3.7933	0.3512 \pm 0.1695

Table 3. Mean squared Chamfer distance and F1 score for multi-view image reconstruction from 300 input views.

5. Applications

5.1. Single-View 3D Reconstruction

Single-view 3D reconstruction aims to infer a full, consistent 3D shape from a single RGB image, a task that is inherently ill-posed due to the loss of depth and occluded geometry. Recent generative models, such as *Hunyuan3D* [28], have demonstrated strong capabilities in synthesizing geometry-consistent multi-view images and depth or normal maps from a single input, effectively recovering plausible 3D structure and texture. Building on these advances, we integrate *VoroLight* with *Hunyuan3D* to transform such multi-view predictions into high-quality volumetric Voronoi meshes suitable for visualization, simulation, and fabrication.

As shown in Fig. 8, from an input front-view RGB image, we use *Hunyuan3D* to generate five additional RGB views (left, right, top, bottom, and back), as well as the corresponding normal fields of these total six views. *VoroLight* then reconstructs the 3D shape by optimizing the Voronoi surface to match six-view silhouette masks and normal fields via differentiable rasterization. After obtaining this refined geometry, the geometry is kept fixed, and a *NDS* is trained on the RGB views to reproduce the predicted appearances on the mesh.

5.2. Artistic Voronoi Lamps

We apply *VoroLight* to the design of artistic Voronoi lamps (Fig. 9): (a,b) heart and sphere lamps from SDF inputs; (c) a cow lamp from a single-view image; and (d) a bunny lamp from a surface target mesh.

For these results, we employ the polygon-face sphere training mode in Stage II for aesthetic purposes. Although this mode introduces slight misalignments between adjacent Voronoi boundary faces, such discrepancies become negligible once the mesh is thickened into a printable wireframe: the edges are thickened into tubes that merge, and the resulting structures appear seamless. For artistic purposes,

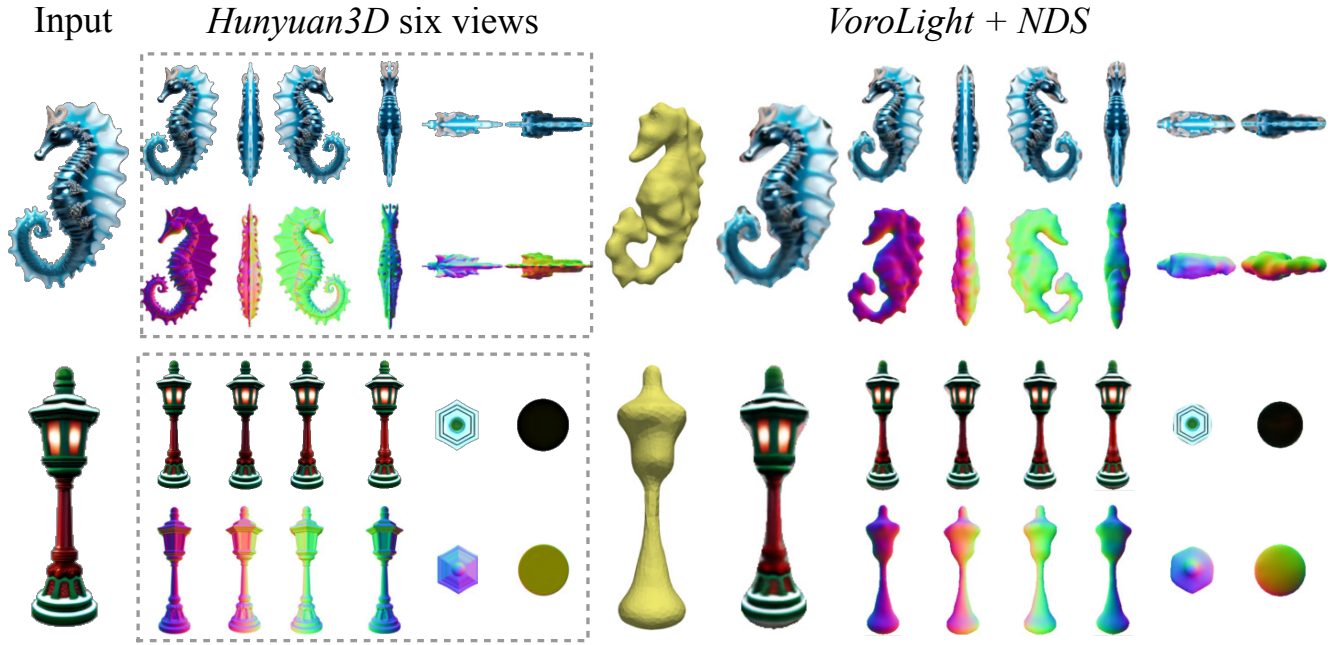


Figure 8. Single-view image shape reconstruction. The example shown here uses $n_{\text{init}} = 40$.

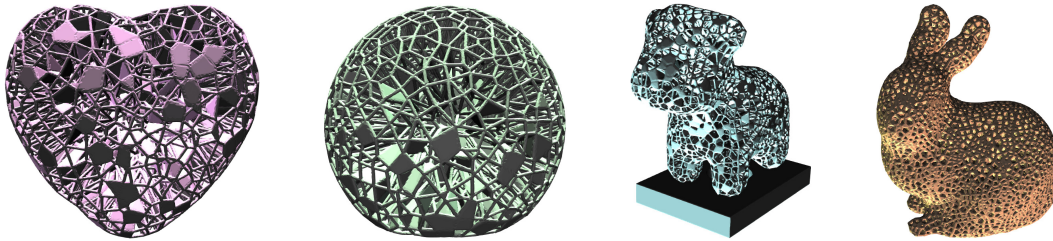


Figure 9. Artistic Voronoi lamp designs: (a) heart lamp, (b) sphere lamp, (c) cow lamp, and (d) bunny lamp, rendered in *ParaView* [2].

we randomly select a subset of Voronoi faces to be solid and extrude them into thin plates, while keeping the remaining faces hollow and defined only by their tubular edges. Small connecting spheres are added at Voronoi vertices to ensure smooth junctions and visual continuity. Additionally, we embed hollow cavities within the input shape to accommodate LED light sources, enabling functional illumination within the printed Voronoi structure.

6. Future Work

Adaptive Cell Density. Incorporating adaptive surface meshing strategies would allow higher Voronoi cell density near sharp edges or high-curvature regions and fewer cells in flatter areas, improving both geometric accuracy and computational efficiency. Likewise, an adaptive volumetric density field can increase internal cell density in regions with complex geometry or physical behavior (e.g., thin structures or stress concentrations) while assigning coarser cells elsewhere. Such control promotes smoother

cell-size gradation from boundary to interior, better integrating the quality objectives of the surface-optimization and volumetric-optimization stages. These behaviors could be realized via gradient-based refinement, hierarchical subdivision, or learned density fields that condition cell placement on geometric, volumetric, or perceptual cues.

Interactive Shape Creation and Simulation. Combining text-to-3D or sketch-based inputs with differentiable Voronoi optimization could enable users to create, sculpt, and deform 3D shapes directly in virtual or augmented reality. The convex structure of volumetric Voronoi cells is naturally suited for physics-based deformation and simulation, allowing real-time mesh manipulation in VR while preserving smooth geometry and topological consistency. The resulting shapes can then be used directly in downstream numerical simulation tasks.

References

- [1] Ahmed Abdelkader, Chandrajit L. Bajaj, Mohamed S. Ebeida, Ahmed H. Mahmoud, Scott A. Mitchell, John D. Owens, and Ahmad A. Rushdi. Vorocrust: Voronoi meshing without clipping. *ACM Trans. Graph.*, 39(3), 2020. 2, 4
- [2] James Ahrens, Berk Geveci, and Charles Law. ParaView: An end-user tool for large data visualization. In *Visualization Handbook*, pages 717–731. Elsevier, Burlington, MA, USA, 2005. 8
- [3] Tianchang Chen, Jun Gao Shen, Sanja Fidler, Qixing Wang, and Lin Gao. Flexicubes: Flexible isosurface extraction for differentiable rendering. In *Proceedings of the IEEE/CVF Conference on Computer Vision and Pattern Recognition (CVPR)*, 2023. 2
- [4] Keenan Crane, Ulrich Pinkall, and Peter Schröder. Robust fairing via conformal curvature flow. *ACM Transactions on Graphics (TOG)*, 32(4):1–10, 2013. 6
- [5] Matt Deitke, Dustin Schwenk, Jordi Salvador, Luca Weihs, Oscar Michel, Eli VanderBilt, Ludwig Schmidt, Kiana Ehsani, Aniruddha Kembhavi, and Ali Farhadi. Objaverse: A universe of annotated 3d objects. In *Proceedings of the IEEE/CVF conference on computer vision and pattern recognition*, pages 13142–13153, 2023. 6
- [6] Q. Du, V. Faber, and M. Gunzburger. Centroidal Voronoi tessellations: Applications and algorithms. *SIAM Review*, 41(4):637–676, 1999. 3, 5
- [7] Mengyuan Ge, Junfeng Yao, Baorong Yang, Ningna Wang, Zhonggui Chen, and Xiaohu Guo. Point2mm: Learning medial mesh from point clouds. *Computers & Graphics*, 115: 511–521, 2023. 2
- [8] Amos Gropp, Lior Yariv, Niv Haim, Matan Atzmon, and Yaron Lipman. Implicit geometric regularization for learning shapes. In *Proceedings of the 37th International Conference on Machine Learning (ICML)*, pages 3569–3579, 2020. 2
- [9] Minghao Guo, Bohan Wang, Kaiming He, and Wojciech Matusik. Tetsphere splatting: Representing high-quality geometry with lagrangian volumetric meshes. *arXiv preprint arXiv:2405.20283*, 2024. 1, 2, 7
- [10] Rana Hanocka, Gal Metzger, Raja Giryes, and Daniel Cohen-Or. Point2mesh: A self-prior for deformable meshes. *arXiv preprint arXiv:2005.11084*, 2020. 2
- [11] Diederik P. Kingma and Jimmy Ba. Adam: A method for stochastic optimization. *CoRR*, abs/1412.6980, 2014. 4
- [12] Samuli Laine, Janne Hellsten, Tero Karras, Yeongho Seol, Jaakko Lehtinen, and Timo Aila. Modular primitives for high-performance differentiable rendering. *ACM Transactions on Graphics*, 39(6), 2020. 7, 2
- [13] Chen-Hsuan Lin, Jun Gao, Luming Tang, Towaki Takikawa, Xiaohui Zeng, Xun Huang, Karsten Kreis, Sanja Fidler, Ming-Yu Liu, and Tsung-Yi Lin. Magic3d: High-resolution text-to-3d content creation. In *Proceedings of the IEEE/CVF conference on computer vision and pattern recognition*, pages 300–309, 2023. 1, 2
- [14] Minghua Liu, Chao Xu, Haiyan Jin, Linghao Chen, Mukund Varma T, Zexiang Xu, and Hao Su. One-2-3-45: Any single image to 3d mesh in 45 seconds without per-shape optimization. *Advances in Neural Information Processing Systems*, 36:22226–22246, 2023. 2
- [15] Xiaoxiao Long, Yuan-Chen Guo, Cheng Lin, Yuan Liu, Zhiyang Dou, Lingjie Liu, Yuexin Ma, Song-Hai Zhang, Marc Habermann, Christian Theobalt, et al. Wonder3d: Single image to 3d using cross-domain diffusion. In *Proceedings of the IEEE/CVF conference on computer vision and pattern recognition*, pages 9970–9980, 2024. 1, 2
- [16] Jiayin Lu, Emanuel A. Lazar, and Chris H. Rycroft. An extension to voro++ for multithreaded computation of voronoi cells. *Computer Physics Communications*, 291:108832, 2023. 6
- [17] Erik Mahieu. Trilateration and the intersection of three spheres. Wolfram Demonstrations Project, 2015. Available at: <https://demonstrations.wolfram.com/TrilaterationAndTheIntersectionOfThreeSpheres/> (accessed DATE). 5
- [18] Nissim Maruani, Roman Klokov, Maks Ovsjanikov, Pierre Alliez, and Mathieu Desbrun. Voromesh: Learning watertight surface meshes with voronoi diagrams. In *Proceedings of the IEEE/CVF International Conference on Computer Vision*, pages 14565–14574, 2023. 2, 3, 6
- [19] Lars Mescheder, Michael Oechsle, Michael Niemeyer, Sebastian Nowozin, and Andreas Geiger. Occupancy networks: Learning 3d reconstruction in function space. In *Proceedings of the IEEE/CVF Conference on Computer Vision and Pattern Recognition (CVPR)*, pages 4460–4470, 2019. 2
- [20] Vincent Nivoliers and Bruno Lévy. Approximating functions on a mesh with restricted voronoi diagrams. In *Computer Graphics Forum*, pages 83–92. Wiley Online Library, 2013. 3
- [21] Logan Numerow, Yue Li, Stelian Coros, and Bernhard Thomaszewski. Differentiable voronoi diagrams for simulation of cell-based mechanical systems. *arXiv preprint arXiv:2404.18629*, 2024. 3, 4
- [22] Jeong Joon Park, Peter Florence, Julian Straub, Richard Newcombe, and Steven Lovegrove. DeepSDF: Learning continuous signed distance functions for shape representation. In *Proceedings of the IEEE/CVF Conference on Computer Vision and Pattern Recognition (CVPR)*, pages 165–174, 2019. 2
- [23] Nikhila Ravi, Jeremy Reizenstein, David Novotny, Taylor Gordon, Wan-Yen Lo, Justin Johnson, and Georgia Gkioxari. Accelerating 3d deep learning with pytorch3d. *arXiv preprint arXiv:2007.08501*, 2020. 6
- [24] Chris H. Rycroft. Voro++: A three-dimensional voronoi cell library in c++. *Chaos*, 19(4):041111, 2009. 6
- [25] Tianchang Shen, Jun Gao, Kangxue Yin, Ming-Yu Liu, and Sanja Fidler. Deep marching tetrahedra: A hybrid representation for high-resolution 3d shape synthesis. In *Advances in Neural Information Processing Systems (NeurIPS)*, pages 6087–6101, 2021. 2
- [26] Hang Si. TetGen, a Delaunay-based quality tetrahedral mesh generator. *ACM Trans. on Mathematical Software*. 41 (2), Article 11, February 2015. 2
- [27] Gabriel Taubin. An accurate algorithm for rasterizing algebraic curves. In *Proceedings on the Second ACM Symposium*

on *Solid Modeling and Applications*, page 221–230, New York, NY, USA, 1993. Association for Computing Machinery. 6

- [28] Tencent Hunyuan3D Team. Hunyuan3d 2.0: Scaling diffusion models for high resolution textured 3d assets generation, 2025. 2, 7
- [29] Peng Wang, Lingjie Liu, Yuan Liu, Christian Theobalt, Taku Komura, and Wenping Wang. Neus: Learning neural implicit surfaces by volume rendering for multi-view reconstruction. *arXiv preprint arXiv:2106.10689*, 2021. 2
- [30] Markus Worchel, Rodrigo Diaz, Weiwen Hu, Oliver Schreer, Ingo Feldmann, and Peter Eisert. Multi-view mesh reconstruction with neural deferred shading. In *Proceedings of the IEEE/CVF Conference on Computer Vision and Pattern Recognition (CVPR)*, pages 6187–6197, 2022. 6, 7, 2
- [31] Yanyang Xiao, Zhonggui Chen, Juan Cao, Yongjie Jessica Zhang, and Cheng Wang. Optimal power diagrams via function approximation. *Computer-Aided Design*, 102:52–60, 2018. 2, 3
- [32] Zibo Zhao, Zeqiang Lai, Qingxiang Lin, Yunfei Zhao, Haolin Liu, Shuhui Yang, Yifei Feng, Mingxin Yang, Sheng Zhang, Xianghui Yang, et al. Hunyuan3d 2.0: Scaling diffusion models for high resolution textured 3d assets generation. *arXiv preprint arXiv:2501.12202*, 2025. 2
- [33] Qingnan Zhou and Alec Jacobson. Thingi10k: A dataset of 10,000 3d-printing models. *arXiv preprint arXiv:1605.04797*, 2016. 6

VoroLight: Learning Quality Volumetric Voronoi Meshes from General Inputs
Supplementary Material



Figure 10. We designed artistic 3D printed lamps using *VoroLight*: (first row) sphere lamp, (second row) heart lamp, (bottom left) bunny lamp, and (bottom right) cow lamp.

A. Detailed Loss Formulations

This section provides the complete mathematical formulations of all loss terms referenced in the main paper.

A.1. Shape Losses

Different input modalities use different shape supervision signals.

Implicit shape level-set field input. Squared L^2 loss normalized by the characteristic length scale h_0 , the grid spacing of the initial discretization:

$$\mathcal{L}_d = \frac{1}{N_{\text{voro}}} \sum_{i=1}^{N_{\text{voro}}} \frac{d(\mathbf{x}_i)^2}{h_0^2},$$

where $d(\mathbf{x}_i)$ is the level-set function value (e.g., signed distance field) evaluated at sample point \mathbf{x}_i on the Voronoi surface. Sample points include face vertices, face centroids, and sub-triangle centers, where sub-triangles are formed by subdividing each Voronoi face by connecting its vertices to its centroid.

Point cloud input & mesh surface input. Mesh surface inputs are converted to an equivalent point-cloud representation by densely sampling points on the surface. Given a target point cloud of the shape, we measure the discrepancy using the bidirectional Chamfer distance:

$$\begin{aligned} \mathcal{L}_{\text{pc}} = & \frac{1}{N_{\text{voro}}} \sum_{i=1}^{N_{\text{voro}}} \min_{\mathbf{y}_j \in \mathcal{P}_{\text{target}}} \|\mathbf{x}_i - \mathbf{y}_j\|^2 \\ & + \frac{1}{N_{\text{target}}} \sum_{j=1}^{N_{\text{target}}} \min_{\mathbf{x}_i \in \mathcal{P}_{\text{voro}}} \|\mathbf{y}_j - \mathbf{x}_i\|^2. \end{aligned} \quad (5)$$

where $\mathcal{P}_{\text{voro}} = \{\mathbf{x}_i\}$ denotes the set of Voronoi surface samples, and $\mathcal{P}_{\text{target}} = \{\mathbf{y}_j\}$ denotes the target surface point cloud.

Image input. Given N_{total} multi-view images, we use a combination of (1) silhouette mask loss $\mathcal{L}_{\text{mask}}$, (2) surface normal map loss $\mathcal{L}_{\text{normal}}$ rendered using the differentiable rasterizer *nvdiffrast* [12], and (3) shading loss $\mathcal{L}_{\text{shading}}$ computed with a learned *neural deferred shader (NDS)* [30].

(1) Silhouette mask loss:

$$\mathcal{L}_{\text{mask}} = \frac{1}{N_{\text{views}}} \sum_{v=1}^{N_{\text{views}}} \text{MSE}(M_{\text{target}}^{(v)}, M_{\text{render}}^{(v)}),$$

where $M_{\text{target}}^{(v)}$ and $M_{\text{render}}^{(v)}$ are the target and rendered binary masks, averaged over $N_{\text{views}} = \min(N_{\text{total}}, 66)$ views per iteration.

(2) Normal map loss:

$$\mathcal{L}_{\text{normal}} = \frac{1}{N_{\text{views}}} \sum_{v=1}^{N_{\text{views}}} \left[\sum_{(i,j) \in \Omega^{(v)}} (1 - \langle \mathbf{n}_{\text{tgt}}^{(v)}(i,j), \mathbf{n}_{\text{rnd}}^{(v)}(i,j) \rangle) \cdot w^{(v)}(i,j) \right]. \quad (6)$$

where $\Omega^{(v)}$ is the set of front-facing pixels; $\mathbf{n}_{\text{tgt}}^{(v)}$, $\mathbf{n}_{\text{rnd}}^{(v)}$ are target/rendered normals in world space; $c_{\text{tgt}}^{(v)} = \langle \mathbf{n}_{\text{tgt}}^{(v)}, \mathbf{d}^{(v)} \rangle$, $c_{\text{rnd}}^{(v)} = \langle \mathbf{n}_{\text{rnd}}^{(v)}, \mathbf{d}^{(v)} \rangle$ with flipped view direction $\mathbf{d}^{(v)}$; and weight $w^{(v)}(i,j) = \exp(|\tilde{c}_{\text{tgt}}^{(v)}(i,j)|) / Z^{(v)}$ where $\tilde{c}_{\text{tgt}}^{(v)} = c_{\text{tgt}}^{(v)}$ if $c_{\text{tgt}}^{(v)} \leq -0.1$, else 0; normalization $Z^{(v)} = \sum_{i,j} \exp(|\tilde{c}_{\text{tgt}}^{(v)}(i,j)|)$ over all pixels.

(3) Shading loss:

$$\mathcal{L}_{\text{shading}} = \frac{1}{N_{\text{valid}}} \sum_{v \in \mathcal{V}_{\text{valid}}} \text{SmoothL1}(\mathcal{F}_{\text{shader}}(\mathbf{p}^{(v)}, \mathbf{n}^{(v)}, \mathbf{d}_{\text{cam}}^{(v)}), \mathbf{c}_{\text{target}}^{(v)}). \quad (7)$$

where $\mathcal{V}_{\text{valid}}$ are views with non-empty masks ($N_{\text{valid}} = |\mathcal{V}_{\text{valid}}|$); $\mathcal{F}_{\text{shader}}$ is a learned *NDS* [30]; $\mathbf{p}^{(v)}$, $\mathbf{n}^{(v)}$, $\mathbf{d}_{\text{cam}}^{(v)}$ are rasterized point position, point normal (both global coordinates), and view direction (surface to camera); evaluated on 75% randomly sampled valid pixels per view; and SmoothL1 is mean over sampled pixels across RGB channels.

A.2. Surface Regularization Losses

To promote geometric smoothness and uniform tessellation on the Voronoi surface, we apply several regularizers. Area, centroid, and Laplacian losses are normalized by mean Voronoi face area \bar{A} .

Normal consistency. Penalizes angular deviation between face normals and their neighborhood average face normal:

$$\mathcal{L}_{\text{normal}} = \frac{1}{N_f} \sum_f (1 - \langle \mathbf{n}_f, \bar{\mathbf{n}}_f \rangle)^2, \quad (8)$$

where N_f is the total number of Voronoi faces, \mathbf{n}_f is the unit normal of face f , and $\bar{\mathbf{n}}_f$ is the normalized average of adjacent face normals.

Area uniformity. Minimizes variance from mean face area:

$$\mathcal{L}_{\text{area}} = \frac{1}{N_f} \sum_f \frac{(A_f - \bar{A})^2}{\bar{A}}, \quad (9)$$

where A_f is the area of face f .

Circularity. We encourage round faces by penalizing low isoperimetric ratios:

$$\mathcal{L}_{\text{circ}} = \frac{1}{N_f} \sum_f (1 - \sigma_f)^2, \quad (10)$$

where $\sigma_f = 4\pi A_f / P_f^2$ is the isoperimetric ratio of face f with area A_f and perimeter P_f . Here, $\sigma_f = 1$ corresponds to a perfect circle.

Centroid alignment. Aligns each face centroid with neighboring face centroids:

$$\mathcal{L}_{\text{centroid}} = \frac{1}{N_f} \sum_f \frac{\|c_f - \bar{c}_f\|^2}{A}, \quad (11)$$

where c_f is the centroid of face f and \bar{c}_f is the average of adjacent face centroids.

Laplacian smoothness. Enforces local averaging of vertex positions:

$$\mathcal{L}_{\text{lap}} = \frac{1}{N_v} \sum_i \frac{\|v_i - \bar{v}_i\|^2}{A}, \quad (12)$$

where N_v is the total number of Voronoi vertices, v_i is the position of vertex i , and \bar{v}_i is the average position of its edge-connected vertex neighbors.

A.3. Volumetric Loss

For volumetric optimization, we adopt a centroidal Voronoi tessellation (CVT) [6] regularizer that encourages each generator to coincide with the centroid of its Voronoi cell:

$$\mathcal{L}_{\text{CVT}} = \frac{1}{N_{\text{inner}}} \sum_{i \in \mathcal{I}} \frac{\|p_i - \bar{c}_i\|^2}{A}, \quad (13)$$

where p_i is the generator position, \bar{c}_i is the centroid of its Voronoi cell (computed as the mean of the cell’s vertex positions), \mathcal{I} denotes the set of deep interior (non-boundary) generator cells, and $N_{\text{inner}} = |\mathcal{I}|$ is the number of deep interior generators. This loss promotes uniform cell volumes and prevents degeneracy in the interior mesh structure.

B. Method Details

B.1. Initialization: Boundary-Reflection Point Sampling

Given an initial bounding box $[a_x, b_x] \times [a_y, b_y] \times [a_z, b_z]$ and a grid resolution parameter n_{init} , we first identify a tight bounding box around the shape, then compute the grid spacing h_0 based on n_{init} applied to the longest side of this tight bounding box, creating a uniform voxel grid with cubic cells of edge length h_0 .

Coarse region classification. We classify each voxel as interior or exterior using a *multi-round random sampling strategy* ($N_{\text{round}} = 35$ samples per voxel) to robustly detect thin features:

- **Implicit field:** Evaluate level-set $d(p) < 0$ for each sample; voxel is interior if any sample is inside.
- **Image:** Project samples to all camera views; voxel is interior if any sample is inside all silhouettes.
- **Mesh:** Cast rays from samples; voxel is interior if any sample’s ray has odd intersection count.
- **Point cloud:** Check samples’ proximity to surface points.

The multi-round sampling is applied in two stages: (i) *coarse tight shape bounding box detection* on a fixed 30^3 grid to identify the minimal axis-aligned bounding box containing the shape; then (ii) *final classification* on the n_{init} -resolution grid within the tight bounding box generates the interior mask \mathcal{M}_{in} , where n_{init} specifies the number of grid cells along the longest side of the tight shape bounding box identified in stage (i), and $h_0 = L_{\text{max}}/n_{\text{init}}$ where L_{max} is the longest dimension of the tight bounding box. We then use morphological dilation to further obtain exterior boundary region \mathcal{M}_{ext} (3-layer band outside \mathcal{M}_{in}).

Boundary-reflection point generation. To generate well-distributed generators near the shape boundary, we use a geometry-aware reflection strategy. First, we place *exterior generators* \mathcal{G}_{ext} at voxel centers within \mathcal{M}_{ext} . To generate corresponding *interior generators* \mathcal{G}_{in} , we compute a signed distance field $d(x)$ from \mathcal{M}_{in} using Euclidean distance. We apply Gaussian smoothing ($\sigma = 1.5$ voxels) to obtain smooth surface normals:

$$\mathbf{n}(x) = \frac{\nabla(G_\sigma * d)(x)}{\|\nabla(G_\sigma * d)(x)\| + \epsilon}, \quad \epsilon = 10^{-8}. \quad (14)$$

For each exterior generator g_{ext} , we compute its distance to the boundary $\delta = |d(g_{\text{ext}})|$ and reflect it inward using the smooth surface normals:

$$g_{\text{in}} = g_{\text{ext}} - 2\delta \cdot \mathbf{n}(g_{\text{ext}}), \quad (15)$$

placing the interior generator at the mirror position. Reflected points are filtered to retain only those strictly inside \mathcal{M}_{in} .

Point filtering. An initial Voronoi diagram is computed on $\mathcal{G}_{\text{in}} \cup \mathcal{G}_{\text{ext}}$, and interior generators are filtered to retain only those whose Voronoi cells intersect the shape boundary (i.e., have faces adjacent to exterior generators). Deep interior generators that do not contribute to the surface are discarded, as Stages I and II focus solely on surface mesh optimization.

B.2. Stage I: Differentiable Voronoi Surface Optimization

Differentiable Voronoi formulation. Following [21], a Voronoi vertex \mathbf{v}_c at the intersection of four generator bisector planes \mathbf{x}_i , $i \in \{0, 1, 2, 3\}$, is computed in closed form as:

$$\mathbf{v}_c = \frac{1}{2} A^{-1} \mathbf{b}, \quad A = \begin{bmatrix} (\mathbf{x}_1 - \mathbf{x}_0)^\top \\ (\mathbf{x}_2 - \mathbf{x}_0)^\top \\ (\mathbf{x}_3 - \mathbf{x}_0)^\top \end{bmatrix}, \quad \mathbf{b} = \begin{bmatrix} \|\mathbf{x}_1\|^2 - \|\mathbf{x}_0\|^2 \\ \|\mathbf{x}_2\|^2 - \|\mathbf{x}_0\|^2 \\ \|\mathbf{x}_3\|^2 - \|\mathbf{x}_0\|^2 \end{bmatrix} \quad (16)$$

This enables back-propagation from vertex-based losses to generator positions \mathbf{x}_i .

Trainable parameters. The generator set consists of interior generators \mathcal{G}_{in} and exterior generators \mathcal{G}_{ext} . Both \mathcal{G}_{in} and \mathcal{G}_{ext} positions are trainable ($N_{\text{train}} = |\mathcal{G}_{\text{in}}| + |\mathcal{G}_{\text{ext}}|$ parameters). The Voronoi surface is extracted as faces separating \mathcal{G}_{in} cells from \mathcal{G}_{ext} cells.

Optimization. We optimize generator positions using Adam [11] with learning rate 5×10^{-4} and ReduceLROnPlateau scheduler (factor 0.5, patience 50 epochs, minimum 10^{-4}). The total loss combines shape matching with geometric regularization:

$$\mathcal{L}_{\text{total}} = w_{\text{shape}} \mathcal{L}_{\text{shape}} + w_{\text{area}} \mathcal{L}_{\text{area}} + w_{\text{normal}} \mathcal{L}_{\text{normal}} + w_{\text{lap}} \mathcal{L}_{\text{lap}} + w_{\text{centroid}} \mathcal{L}_{\text{centroid}} + w_{\text{circ}} \mathcal{L}_{\text{circ}}. \quad (17)$$

Adaptive remeshing. To avoid expensive recomputation, we cache Voronoi connectivity and remesh only when maximum generator displacement $\Delta_{\text{max}} = \max_i \|\mathbf{x}_i^{(t)} - \mathbf{x}_i^{(t_{\text{last}})}\| \gg 0.1 \cdot h_0$. Otherwise, we update only vertex positions using the differentiable formula. Remeshing typically occurs every 5–20 iterations early in training, and every 50–100 iterations near convergence.

Point re-categorization. Every 100 epochs, we re-categorize generators that have drifted: generators surrounded by opposite-category neighbors swap categories to maintain spatial clustering of \mathcal{G}_{in} and \mathcal{G}_{ext} , followed by full remeshing.

B.3. Stage III: Interior Point Generation Details

For volumetric mesh generation, we want N_{inner} deep interior generator points in addition to the surface generators \mathcal{G}_1 (inner) and \mathcal{G}_2 (outer) obtained from Stage II. A critical constraint is that adding interior generators must *not alter the surface mesh* that was optimized in Stage II. A naive approach of randomly sampling points inside the mesh would fail: while such points may be geometrically inside the

shape, their Voronoi cells can still intersect the surface tessellation between \mathcal{G}_1 and \mathcal{G}_2 , thereby modifying the Stage II result. We employ a *Voronoi-verified iterative generation* strategy that explicitly filters out any candidate whose Voronoi cell would intersect the surface.

Candidate generation. From Stage II, we obtain a triangulated surface mesh $\mathcal{M} = (\mathbf{V}, \mathbf{F})$ by subdividing each Voronoi polygon face into triangles. We compute the mesh’s tight bounding box $[\mathbf{m}_{\text{min}}, \mathbf{m}_{\text{max}}]$, which is typically much tighter than the global domain $[a_x, b_x] \times [a_y, b_y] \times [a_z, b_z]$, improving sampling efficiency.

At each outer iteration k , we generate $N_{\text{cand}}^{(k)} = \max(200, 3 \cdot N_{\text{remain}}^{(k)})$ candidate points by uniform random sampling in the mesh bounding box, where $N_{\text{remain}}^{(k)}$ is the number of points still needed. We over-generate ($3\times$) to compensate for candidates outside the mesh and candidates that violate the fixed boundary, which will be deleted.

Iterative Voronoi filtering. For each batch of candidates $\mathcal{C}^{(k)}$, we perform an inner iterative refinement to ensure no Voronoi boundary violations remain:

1. Initialize $\mathcal{C}_{\text{filtered}}^{(0)} = \mathcal{C}^{(k)}$.
2. At inner iteration j , construct temporary generator set $\mathcal{G}_{\text{temp}}^{(j)} = \mathcal{C}_{\text{filtered}}^{(j)} \cup \mathcal{G}_1 \cup \mathcal{G}_2$ and compute Voronoi diagram.
3. Designate the first $|\mathcal{C}_{\text{filtered}}^{(j)}| + |\mathcal{G}_1|$ generators as shape points and \mathcal{G}_2 as exterior points. The Voronoi algorithm identifies boundary generator indices $\mathcal{I}_{\text{bdry}}^{(j)}$.
4. Remove candidates in $\mathcal{I}_{\text{bdry}}^{(j)}$: $\mathcal{C}_{\text{filtered}}^{(j+1)} = \mathcal{C}_{\text{filtered}}^{(j)} \setminus \mathcal{I}_{\text{bdry}}^{(j)}$.
5. Repeat until $\mathcal{I}_{\text{bdry}}^{(j)} = \emptyset$ or maximum 50 inner iterations reached.

This iterative approach ensures that removing boundary points doesn’t create new boundary violations in the updated Voronoi diagram.

Accumulation and optimization. We accumulate verified deep interior points across outer iterations until $|\mathcal{G}_{\text{inner}}| \geq N_{\text{inner}}$, then trim to exactly N_{inner} points. The final generator set is $\mathcal{G}_{\text{vol}} = \mathcal{G}_{\text{inner}} \cup \mathcal{G}_1 \cup \mathcal{G}_2$, where only $\mathcal{G}_{\text{inner}}$ are optimized in Stage III using the CVT loss, while $\mathcal{G}_1 \cup \mathcal{G}_2$ remain fixed. This ensures the Stage II surface is preserved exactly while optimizing volumetric mesh quality.

C. Ablation

C.1. Volumetric mesh resolution

Figure 11 shows volumetric meshes generated with different deep inner-point counts N_{init} , following the procedure described in Sec. B.3. The inner cells remain uniform and rounded, regularized by the CVD loss. However, because the surface cells are denser, the transition in element size

from boundary cells to interior cells is not gradual. This discrepancy is reduced as the number of inner points increases and the volumetric resolution becomes closer to that of the surface. In future work, adaptive-density deep inner points could be sampled to provide smoother gradation of mesh elements—denser near the boundary and coarser in the deep interior of the shape.

C.2. Initial grid resolution

As described in Sec. B.1, n_{init} denotes the number of initial grid cells along the longest side of the shape, where the initialization is a uniform cubic grid.

Figure 12 shows the effect of varying this initial resolution. Across all settings, our method consistently converges to a smooth and watertight surface mesh, demonstrating strong robustness to coarse initialization. As the resolution increases, finer geometric details are recovered more faithfully. For the unicorn (left), higher-resolution initializations better capture thin structures such as the horn. For the lion model (right), the improvement is especially visible in slender regions: the tail, which may appear partially disconnected at low resolutions, becomes fully connected and anatomically coherent at higher resolutions; the legs and undercut regions start to form cleaner openings; and the curvature of the torso becomes smoother and more accurately defined.

D. More Results

We present more shape reconstruction results from target mesh surface inputs in Fig. 13, from 300-view image inputs in Fig. 14, and from single-view image inputs in Fig. 15.

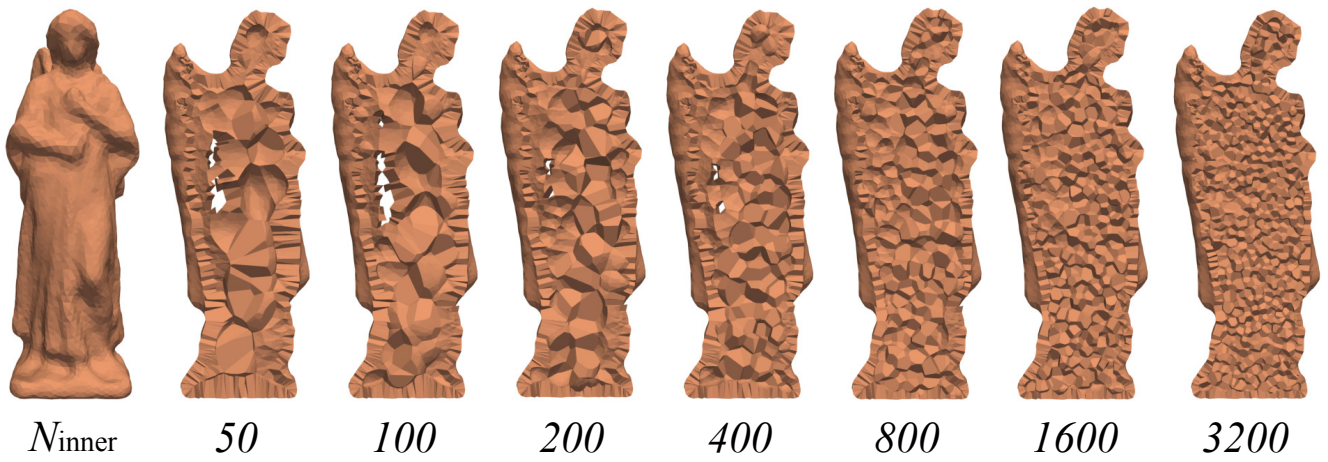


Figure 11. Ablation on the volumetric mesh resolution with varying numbers of deep inner points N_{init} . The surface mesh obtained uses $n_{\text{init}} = 25$.

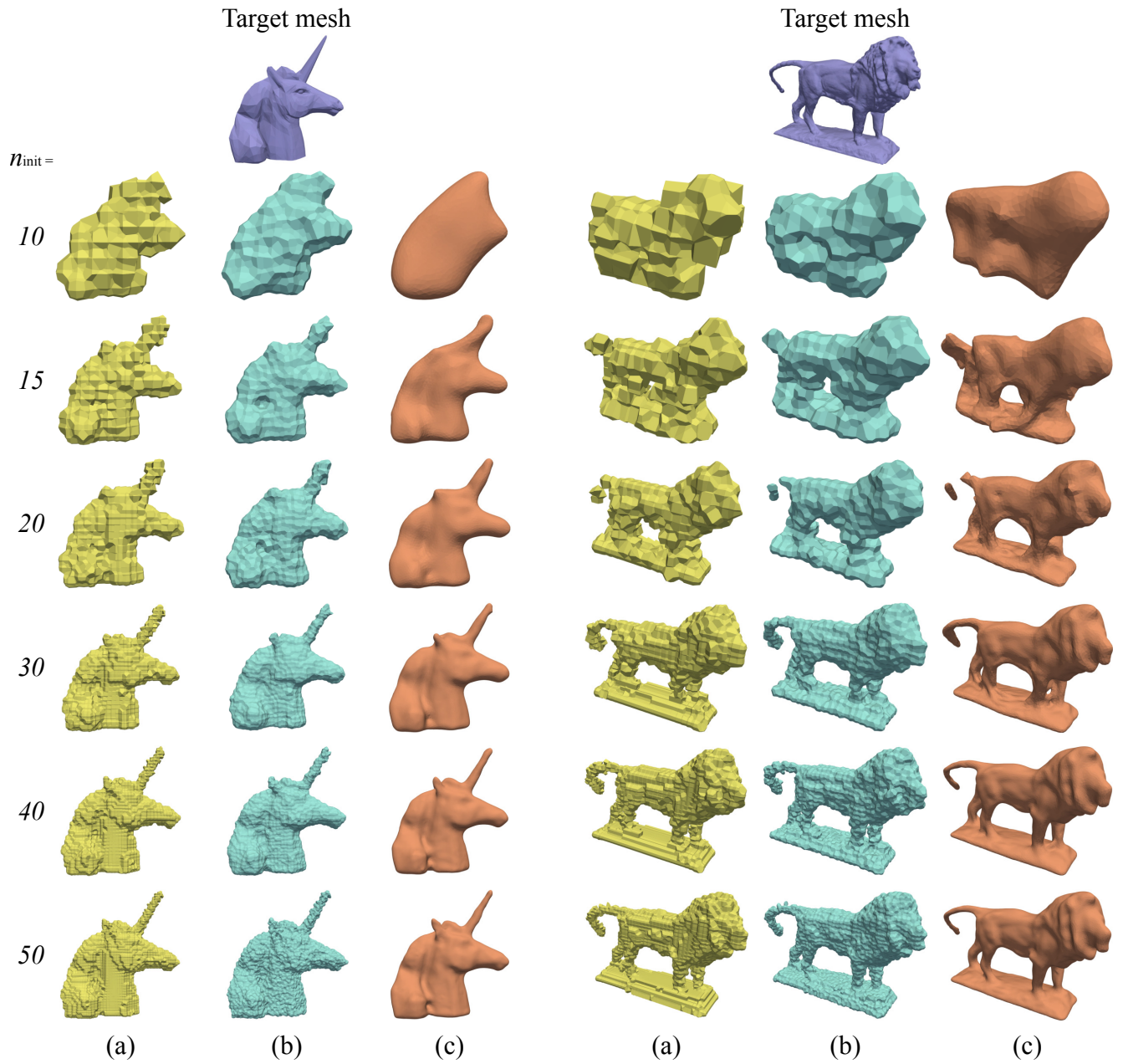


Figure 12. (a) Initial Voronoi mesh. (b) Optimized Voronoi polygon surface after Stage I. (c) Optimized Voronoi surface after Stage II, using the triangular-sphere refinement scheme.

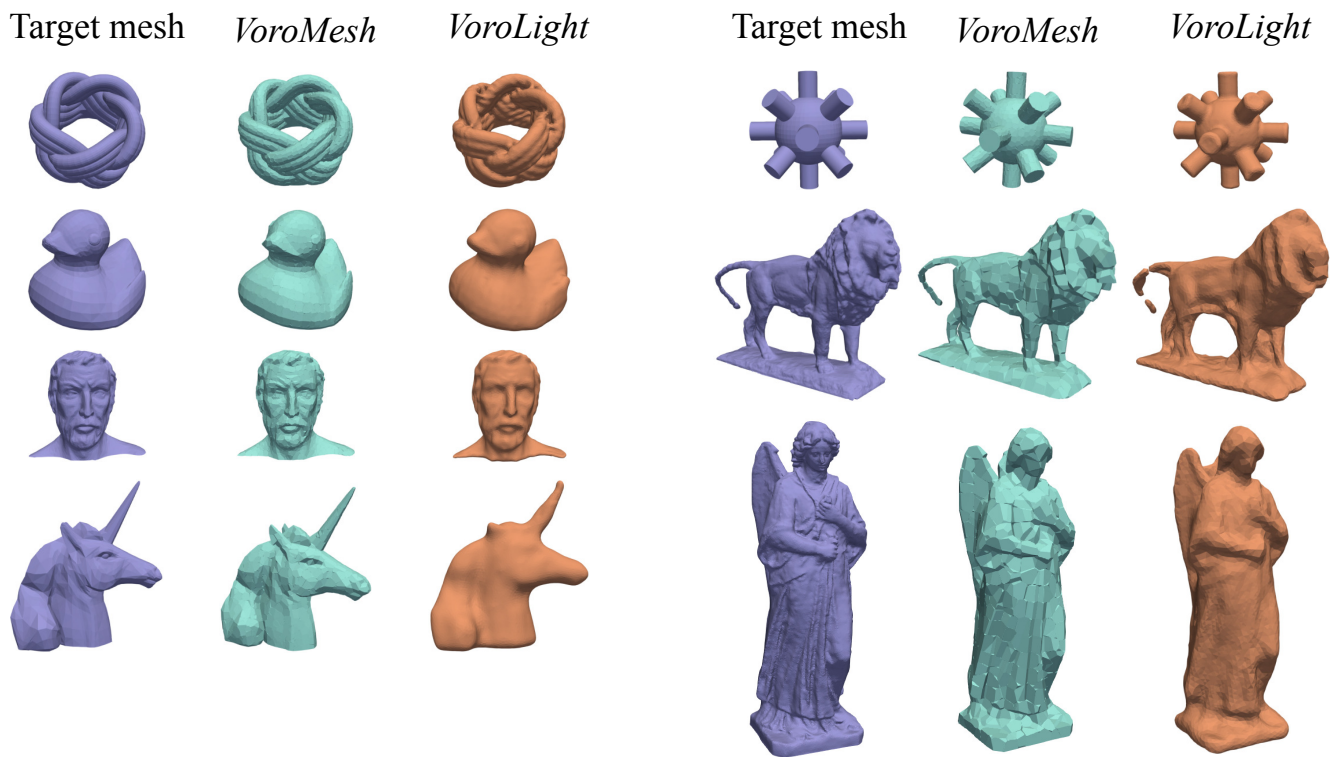


Figure 13. Comparison with *VoroMesh* using mesh inputs. As discussed in Sec. 4.2, *VoroLight* tends to smooth certain shape features but achieves near-perfect alignment of surface Voronoi faces, whereas *VoroMesh* better preserves fine geometric details at the cost of slight misalignments between adjacent faces. The example shown here uses $n_{\text{init}} = 25$.

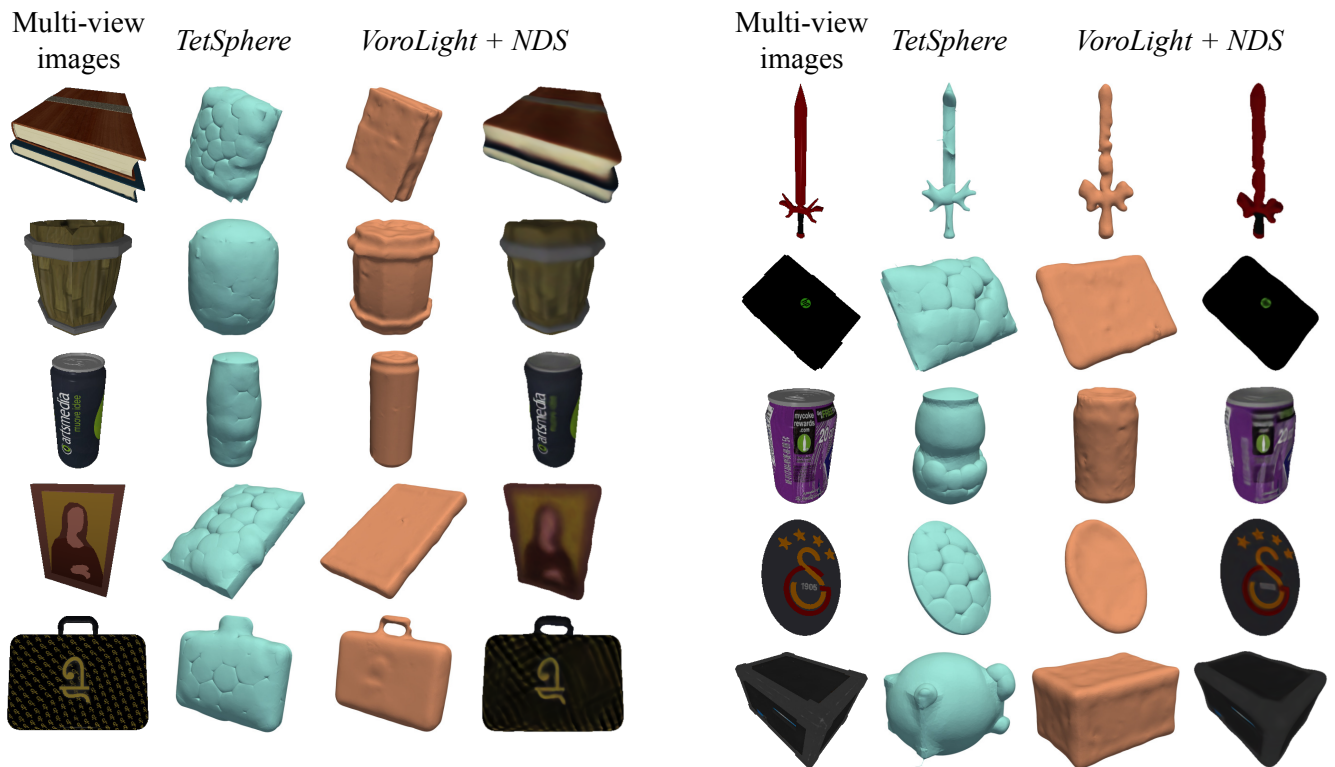


Figure 14. Comparison with *TetSphere* using 300-view image inputs. As discussed in Sec. 4.3, *VoroLight* reconstructs watertight volumetric meshes with globally consistent topology, whereas *TetSphere* represents shapes using locally volumetric tetrahedral meshes organized as disconnected tetrahedral clusters. The example shown here uses $n_{\text{init}} = 40$.



Figure 15. More results using single-view image inputs. As discussed in Sec. 5.1, we first use *Hunyuan3D* to generate consistent six-view images of the target shape, and use *VoroLight* to obtain the reconstructed shape. Afterwards, a neural deferred shader (*NDS*) is trained to obtain the target RGB appearances. The example shown here uses $n_{\text{init}} = 40$.